Optimal Voice Coil Actuators for Needle-free Jet Injection

Bryan P. Ruddy[1*], *Member, IEEE*, Ian W. Hunter[2], *Member, IEEE*, and Andrew J. Taberner[1], *Member, IEEE*

***Abstract*— We present a scaling model for electrically-actuated needle free jet injectors, establishing the relationship between injection volume and motor size. Using an analytical electromagnetic model for the motor, we derive an optimal motor design, and show that this design is approximately scale-invariant. To illustrate the utility of this model, we then describe the design of a motor for use with 300 μL disposable injection ampoules with a mass of just 300 g, including a light-weight support structure. Experimental verification of the motor performance shows close agreement to model predictions, with a peak force of 1000 N/kg and a 150 m/s water jet delivered.**

I. Introduction

Needle-free jet injection is a promising technique for drug delivery using a >100 m/s stream of liquid drug, capable of penetrating skin and underlying tissue to depths ranging from epidermal to intramuscular [1]. Formation of this jet requires pressures of over 20 MPa, yet the jet is only required for tens of milliseconds in order to penetrate the skin. As the penetration depth is very sensitive to jet velocity [2], control of the depth requires force control with better than 1 kHz bandwidth.

There have been several efforts to construct jet injectors with actuators that can provide this high-bandwidth control, including voice coils [3], [4], mechanically-amplified piezoelectric actuators [5], and even pulsed lasers [6]. While able to achieve the goal of jet velocity control, these devices suffer from a number of drawbacks: piezoelectric and laser pulse systems are limited in the total drug volume they can deliver, while voice coil systems are relatively large and heavy for hand-held medical devices.

To date, there have been no comprehensive studies of actuator design in the context of liquid jet delivery. While dynamic models of injector behavior have been developed for spring powered [7] and voice coil powered injectors [8], [9], these models do not address the design of the actuator. Instead, these models treat the actuator as an ideal device, and cannot predict the size or weight of actuator that might be required.

Here, we present a basic scaling model of the jet delivery process, and couple it to an electromagnetic analysis of a voice coil actuator. By minimizing the power consumption of the actuator at a fixed actuator mass, while allowing the piston diameter, stroke length, and actuator internal dimensions to vary, we show that the optimal voice coil design for jet delivery is scale invariant. We then validate this design method by demonstrating jet delivery by a motor built to its specifications.

This work was supported in part by the University of Auckland Faculty Research Development Fund.

[1]B. P. Ruddy and A. J. Taberner are with the Auckland Bioengineering Institute and the Department of Engineering Science, University of Auckland, Auckland 1142 New Zealand (phone: +64 9 923 2424 email: b.ruddy@auckland.ac.nz; a.taberner@auckland.ac.nz)

[2]I. W. Hunter is with the Department of Mechanical Engineering, Massachusetts Institute of Technology, Cambridge, MA 02139 USA (email: ihunter@mit.edu)

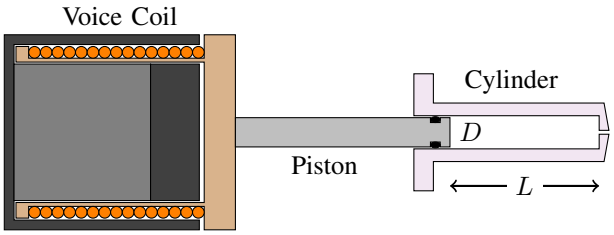

Fig. 1. A basic schematic of a voice-coil-driven jet apparatus. The maximum working length of the cylinder, L, is typically also equal to the maximum usable stroke of the actuator; the relative values of the cylinder diameter D and the working length determine the power required to operate the system.

II. Scaling of Jet Production

Fig. 1 shows a simplified schematic of a jet-producing apparatus, with a fluid-filled cylinder, an output nozzle, and a voice coil actuator driving a piston in the cylinder. For simplicity, we will ignore the influence of friction; it has been shown in the context of jet injection [5], [7] that friction has little influence on steady-state jet production. (Furthermore, inclusion of friction via an orifice discharge coefficient [10] does not alter the scaling relationships.) In this case, the actuator force F and the jet velocity v can be related as follows:

$$F = \frac{\pi}{8}\rho v^2 D^2, \tag{1}$$

where ρ is the density of the fluid being delivered and D is the diameter of the cylinder.

We can then combine this relation with a scaling model for the actuator so as to determine the power and energy required for jet production. For permanent magnet motors, the energy conversion efficiency is described by the motor constant K_m, the ratio of the force developed to the square root of the power dissipated. This leads directly to an expression for the power dissipation P required for jet production by a permanent magnet motor:

$$P = \frac{\rho^2 V^2 v^4}{4K_m^2 L^2}, \tag{2}$$

where V is the volume to be delivered and L is the working length of the cylinder, as well as the stroke length of the motor. This scaling relationship suggests that a combination of a small delivery volume and a very high-performance

978-1-4244-7929-0/14/$26.00 ©2014 IEEE

motor are required for physically reasonable systems. For instance, the delivery of 1 mL of water at 150 m/s from a cylinder 30 mm long, using a motor specified at $10\,\mathrm{N}/\sqrt{\mathrm{W}}$, requires 1400 W of power.

In order to complete the scaling picture, we need to have some idea of the relationship between motor size and motor constant. It can be shown [11] that the motor constant scales with the square root of the motor mass M:

$$K_m = B_{rem}\hat{K}_m\sqrt{\frac{\sigma M}{\rho_c}}, \tag{3}$$

where B_{rem} is the remanence of the permanent magnets, σ and ρ_c are the electrical conductivity and density of the wire conductor (typically copper), and $\hat{K}_m$ is a dimensionless parameter describing the internal magnetic and electric geometry of the motor. (Note that non-dimensionalized quantities throughout this paper are denoted by hats.) We can thus determine the overall scaling behavior for the jet-production system, neglecting constant factors and material properties:

$$P \propto \frac{V^2 v^4}{ML^2\hat{K}_m^2}. \tag{4}$$

Typically, ρ, V, v, and d are determined by the application of the jet, and the power P is limited by the power amplifier, but the aspect ratio of the cylinder (i.e. L) can be freely varied and minimization of the actuator mass M is desired.

For voice coils, the stroke length is closely related to the relative magnet dimensions, which in turn determine $\hat{K}_m$. Thus, there may be an optimum choice for L that minimizes P for a given mass. (For other motor types that employ a spatially periodic structure, this linkage is absent; the scale of the repeat units and the number of units employed are independent design parameters, and the mass can be minimized by designing as long a motor as is practical.) To determine the optimum stroke, we will need to couple the scaling model to an electromagnetic model that can determine $\hat{K}_m$.

III. Electromagnetic Model

In order to determine an appropriate voice coil electromagnetic model, we must first select the general motor topology of interest. Traditional voice coil actuators employ a topology with magnets and an iron pole piece located centrally within an iron casing that serves as a flux return path. As the iron pole piece may pose saturation and demagnetization problems at high currents (and thus high forces), we instead chose to consider a quasi-Halbach topology, as shown in Fig. 2, that replaces the iron pole piece with a set of radially-oriented magnets. The symmetric motor structure shown here eliminates fringing fields and thereby uses its magnets more efficiently.

The quasi-Halbach motor can be directly modeled via Maxwell's equations, if the iron can be considered infinitely permeable—the endcaps enforce periodic boundary conditions, and models developed for slotless linear synchronous motors can be used, e.g. [11]–[13]. Here, we will briefly illustrate a numerically stable analytical model for the quasi-Halbach voice coil based on the modified Struve function [14]. Finite element models will also be presented to provide guidance as to the validity of the infinite-permeability assumption.

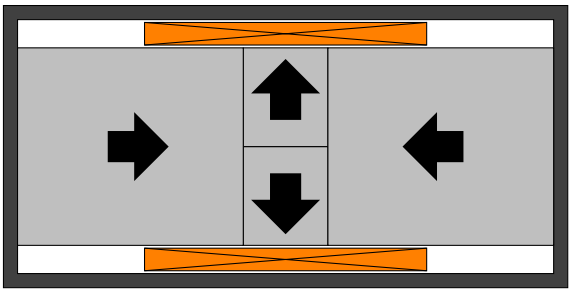

Fig. 2. In this quasi-Halbach motor topology, the coil (orange) is mechanically connected to the load via supports that penetrate one end cap (not shown). (Arrows indicate the direction of magnetization in the permanent magnets.)

A. Semi-Analytical Model

Due to the linear behavior of rare earth permanent magnets [15], we can directly use a Fourier series solution of Maxwell's equations to determine the motor performance from its dimensions. Let the length of the radial magnets be given by $2L_r$ and the length of the axial magnets be L_m; we can then define the length ratio $\delta \equiv L_r/(L_r + L_m)$. Following the procedure in [16], we can determine the magnetization components

$$\hat{M}_{rn} = \frac{2}{n\pi}\sin\left(\frac{n\pi\delta}{2}\right)\left((-1)^{n+1}+1\right), \tag{5}$$

$$\hat{M}_{zn} = -\frac{2}{n\pi}\cos\left(\frac{n\pi\delta}{2}\right)\left((-1)^{n+1}+1\right), \tag{6}$$

where $\hat{M}_{rn}$ and $\hat{M}_{zn}$ are the dimensionless radial and axial magnetizations, respectively, at harmonic order n, and the spatial wavenumber k is given by $k = \pi/(2L_m + 2L_r)$. The symmetry of the motor dictates the absence of even harmonics from the magnetization pattern.

The solutions to Maxwell's equations for this set of boundary conditions and magnetizations can be most expediently written in terms of a function based upon the modified Bessel function of the first kind $\mathrm{I}_\nu(x)$ and the modified Struve function $\mathrm{L}_\nu(x)$,

$$\Lambda_\nu(x) \equiv \frac{\pi}{2}\big(\mathrm{I}_\nu(x) - \mathrm{L}_\nu(x)\big), \tag{7}$$

that possesses computationally efficient series representations [17]. To solve for the field coefficients, it is helpful to define a further set of auxiliary functions:

$$\mathcal{L}_\mathrm{I}(x) \equiv x\left(\Lambda_1(x)\,\mathrm{I}_0(x) - \Lambda_0(x)\,\mathrm{I}_1(x)\right), \tag{8}$$

$$\mathcal{L}_\mathrm{K}(x) \equiv x\left(\Lambda_1(x)\,\mathrm{K}_0(x) + \Lambda_0(x)\,\mathrm{K}_1(x)\right), \tag{9}$$

where $\mathrm{K}_\nu(x)$ is the modified Bessel function of the second kind. These functions are closely related to the integrals of

the modified Bessel functions of zero order [17]. The field coefficients in the coil region can then be found as

$$b_n = \hat{M}_{rn}\,\mathcal{L}_{\mathrm{I}}(nkr_m) - nkr_m\hat{M}_{zn}\,\mathrm{I}_1(nkr_m)\,, \tag{10a}$$

$$a_n = b_n\frac{\mathrm{K}_0(nkr_{fi})}{\mathrm{I}_0(nkr_{fi})}, \tag{10b}$$

where the field harmonic components in the radial and axial directions are given by

$$\hat{B}_{rn} = \quad a_n\,\mathrm{I}_1(nkr) + b_n\,\mathrm{K}_1(nkr) \ \text{ and} \tag{11a}$$

$$\hat{B}_{zn} = -a_n\,\mathrm{I}_0(nkr) + b_n\,\mathrm{K}_0(nkr)\,, \tag{11b}$$

respectively, r_m is the radius of the magnets, and r_{fi} is the radius at the inside of the iron shell.

With the magnetic field completely defined, the force produced by the motor can be determined by integrating the radial component of the field over the coil volume:

$$F = B_{rem}J\sum_{n=1}^{\infty}\frac{2\pi\hat{f}_n}{n^3k^3}\left(\sin nk\left(z_c' + \frac{L_c}{2}\right) - \sin nk\left(z_c' - \frac{L_c}{2}\right)\right), \tag{12}$$

$$\hat{f}_n \equiv a_n\left(\mathcal{L}_{\mathrm{I}}(nkr_{co}) - \mathcal{L}_{\mathrm{I}}(nkr_{ci})\right) - b_n\left(\mathcal{L}_{\mathrm{K}}(nkr_{co}) - \mathcal{L}_{\mathrm{K}}(nkr_{ci})\right), \tag{13}$$

where z_c' is the coil position with zero defined to be centered in the motor, L_c is the length of the coil, and r_{ci} and r_{co} are the radii at the inner and outer edges of the coil, respectively.

In order to determine the dimensionless motor constant $\hat{K}_m$, we also need to determine expressions for the power dissipation and mass of the motor. The power can be calculated easily from the coil volume,

$$P = \frac{\pi L_c J^2\left(r_{co}^2 - r_{ci}^2\right)}{\sigma}, \tag{14}$$

but in order to find the motor mass we must estimate the thickness of the iron shell. We can do so by first determining the maximum flux in the iron shell, then calculating the cross-sectional area needed for a given saturation flux density B_{sat}. The flux can be determined by integrating the radial field over half of the motor length:

$$\Phi_0 = r_{fi}B_{rem}\sum_{n=1}^{\infty}\frac{2\pi\,(-1)^{\frac{n-1}{2}}}{nk}\left[a_n\,\mathrm{I}_1(nkr_{fi}) + b_n\,\mathrm{K}_1(nkr_{fi})\right]. \tag{15}$$

The overall motor mass can then be calculated as

$$M = 2\pi\rho_m r_m^2\left(L_m + L_r\right) + \pi\rho_c L_c\left(r_{co}^2 - r_{ci}^2\right) + \frac{2\rho_f\Phi_0}{B_{sat}}\left(L_m + \frac{\Phi_0}{\pi r_m B_{sat}} + L_r\right) + \frac{2\rho_f\Phi_0 r_{fi}^2}{r_m B_{sat}}, \tag{16}$$

where ρ_m and ρ_f are the densities of the magnet and iron, respectively. Finally, while the governing equations themselves can be non-dimensionalized, in this case it is more convenient to use the definition of the motor constant to determine $\hat{K}_m$:

$$\hat{K}_m = \frac{F}{B_{rem}}\sqrt{\frac{\rho_c}{\sigma MP}}. \tag{17}$$

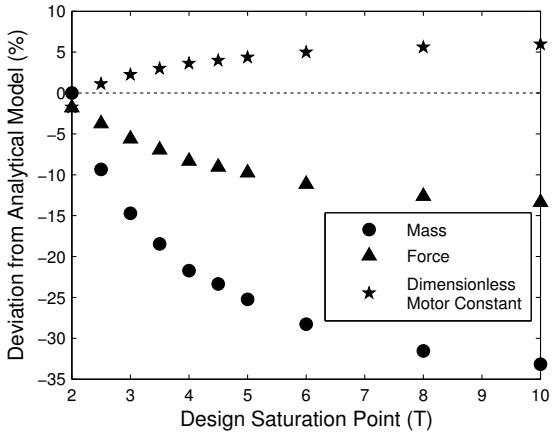

Fig. 3. Forcing saturation of the iron components of a quasi-Halbach motor results in an improved dimensionless motor constant due to reduced mass. (The performance reference is calculated for B_{sat} = 2 T.)

B. Iron Saturation

The performance of this analytical modeling approach in describing ironless motors has been illustrated in [11], [16], but a key issue in applying the method to voice coils is the choice of nominal saturation flux density B_{sat}. Choosing a low saturation flux makes the motor heavy, while choosing a higher value may reduce force production.

To illustrate this effect, Fig. 3 shows the relative performance at mid-stroke and low current density ($10^6\,\mathrm{A/m^2}$) for a motor with $r_m = 10\,\mathrm{mm}$, $r_{fi} = 13\,\mathrm{mm}$, $r_{ci} = 10.5\,\mathrm{mm}$, $r_{co} = 12.9\,\mathrm{mm}$, $L_r = 5\,\mathrm{mm}$, $L_m = 35\,\mathrm{mm}$, and $L_c = 40\,\mathrm{mm}$ over a range of different nominal saturation fluxes, as calculated via finite element analysis (FEA). (The magnets are given a remanence of $B_{rem} = 1.334\,\mathrm{T}$.) For these dimensions, the best motor performance at mid-stroke is obtained when the iron is entirely removed; the mass penalty due to iron is slightly more significant than the reduction in force production from removing it. Allowing the iron to be saturated also tends to reduce the reluctance force near the ends of the stroke [14]; as a compromise, the remaining analyses and designs use $B_{sat} = 4.0\,\mathrm{T}$.

C. Optimization

Using Eqn. 17 for the dimensionless motor constant and Eqn. 4 for the power required to perform an injection, we are equipped to determine the power-optimal motor design. The natural choice of objective function is to maximize the product $L\hat{K}_m$ for a fixed motor mass, as increasing the motor size always reduces the power requirement. The remaining free parameters for the motor design are r_m, r_{fi}, δ, L, and L_c; we set the coil radii based on fixed clearance distances (0.5 mm inside and 0.1 mm outside) from the magnet and iron shell. (A more detailed version of the electromagnetic model allows for hollow magnets, the effect of practical segmented radial magnets, and the fill factor of the coil winding [14], parameters that are also held fixed for optimization.)

Fig. 4 illustrates the results of this optimization process, based on the motor constant with the coil positioned at

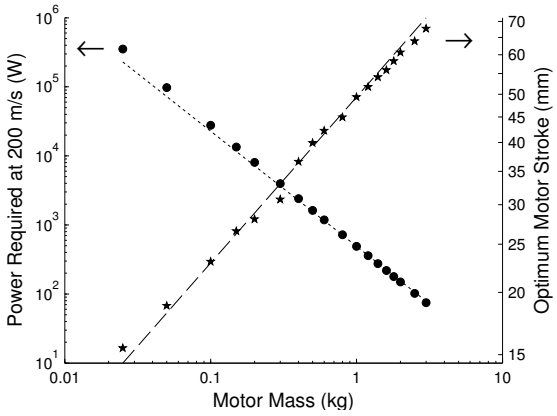

Fig. 4. The optimum stroke length (right) scales with the linear size of the motor: stars indicate optimization results, while the dotted line is a guide to the eye proportional to $M^{1/3}$. Using the optimized dimensions for a motor that delivers a volume of 300 μL, the power required to deliver a 200 m/s jet is shown by dots via the left axis, with a guide line proportional to $M^{-5/3}$.

the quarter-stroke position, $z_c' = L/4$. (Optimization at mid-stroke favors motors with large variations in motor constant over the stroke, while optimization at the end of the stroke sacrifices a large amount of average motor constant to provide very modest improvements in the minimum motor constant.) The optimal value of L scales with the linear dimensions of the motor, or as $M^{1/3}$, in spite of the fixed clearance distances, as do the other geometric parameters. So long as the clearance is small enough to ignore, there is a single optimal configuration for a quasi-Halbach voice coil with a scale-invariant dimensionless motor constant. The dimensions can thus be selected based on the desired motor mass. As a result, the overall power required scales as $M^{-5/3}$, deviating slightly at low masses due to the more deleterious effect of the clearance gaps in small motors.

IV. Injector Design

Using the optimization results, the motor design appropriate for an off-the-shelf ampoule (Injex part #100100, 30 mm stroke, 300 μL volume) was selected. The resulting motor dimensions are $r_m = 8.00\,\text{mm}$, $r_{fi} = 12.71\,\text{mm}$, $r_{fo} = 13.48\,\text{mm}$, $r_{ci} = 8.50\,\text{mm}$, $r_{co} = 12.61\,\text{mm}$, $L_r = 3.80\,\text{mm}$, $L_m = 36.0\,\text{mm}$, and $L_c = 39.8\,\text{mm}$, with a 3.8 mm central hole through the magnets (grade N42SH) to allow for structural support, and end caps 1.25 mm thick. The detailed model predicts a motor constant of $3.6\,\text{N}/\sqrt{\text{W}}$ for this configuration, and a motor mass of 230 g neglecting structural components. A coil winding of 624 turns of 25 AWG wire with heavy-build insulation was selected, giving a fill factor of 62%, a coil resistance of 4.4 Ω, and a predicted force constant of 7.6 N/A. (Including the effect of saturation via FEA gives a motor constant of $3.1\,\text{N}/\sqrt{\text{W}}$, and a resulting force constant of 6.4 N/A.)

In order to support the electromagnetic components of the motor, as minimal a support structure as practical is desired. Our solution is illustrated in Fig. 5, a cut-away rendering of the complete injector. The iron end cap closest to the

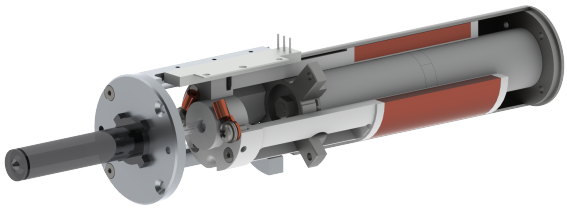

Fig. 5. A cut-away view of the optimized motor design, showing the bobbin and end-cap structure (center) as well as the drug ampoule (left) and position sensor (top center).

ampoule has been shaped as a cross, with the arm thickness increased to provide the correct total cross-sectional area of iron for the specified saturation flux density. The coil bobbin has a matching set of slots, allowing motion to be transmitted beyond the end cap; for assembly, the end cap is slipped through the slots and rotated into place. The motor is held together by a non-magnetic M3 threaded rod that passes through the magnets' central hole. The ampoule is secured to the motor by an aluminum cage that also holds a linear potentiometer (ALPS RDC10) used to sense the motor position. Electrical connection to the coil is made via flexible wires coiled inside the cage and exiting adjacent to the potentiometer.

V. Results and Discussion

The complete injector system has a mass of 300 g, including the ampoule and piston. Including a plastic case (Fig. 6), trigger, and ancillary components, the resulting injector handpiece has a mass of just 426 g, less massive than the motor alone from [4].

The motor, as built, exhibits a force constant of 6.7 N/A, as determined by back-EMF measurement at zero current. This compares favorably with the FEA prediction, and is only 12% lower than the prediction of the analytical model. The performance was likely helped by the use of thicker end-caps than called for by the model, due to mechanical strength and manufacturing considerations.

The dynamic performance of the injector was measured using a current-controlled capacitor discharge system, for currents up to 45 A. Acceleration measurements of the unloaded motor and direct force measurements using a load cell were consistent with the zero-current force constant for all currents tested. The behavior of the injector is illustrated by Fig. 7, showing the ejection of water from the ampoule at a jet velocity of 150 m/s. (The jet velocity is estimated from the coil position and the piston-nozzle area ratio of 381:1.) The initial velocity peak is caused by the compliance of the piston and ampoule and the abrupt current rise time.

VI. Future Directions

This work has provided guidance as to the relationship between jet injector delivery volume, voice coil size, and power consumption, based on the performance of an optimal voice coil design. For larger delivery volumes, as might be required for veterinary jet injector use, the model implies that an impractically large actuator with a mass of several

Fig. 6. The complete jet injector hand-piece has a mass of 426 g, and is connected to its power amplifier via the cable in the handle.

kilograms is required. In order to build voice-coil-powered injectors for large volumes, then, we must explore new mechanical designs that can break the coupling between the stroke length and the force required for a particular jet velocity.

For small injection volumes, a miniaturized power amplifier capable of a 10 kW output (albeit briefly) is needed to enable a self-contained hand-held jet injector. Work is underway to develop such a system from the current source used to test our voice coil, along with an accompanying high-bandwidth position control system.

Acknowledgment

The authors thank Linh Do for his assistance with the visual design and style of the jet injector hand-piece, and James McKeage for his assistance with its fabrication. The authors also thank Stephen Olding for his assistance in manufacturing the voice coil motor.

References

[1] S. Mitragotri, "Current status and future prospects of needle-free liquid jet injectors," *Nature Rev. Drug Discovery*, vol. 5, pp. 543–548, July 2006.

[2] J. Schramm-Baxter and S. Mitragotri, "Needle-free jet injections: dependence of jet penetration and dispersion in the skin on jet power," *J. Controlled Release*, vol. 97, pp. 527–535, 2004.

[3] B. D. Hemond, A. Taberner, C. Hogan, B. Crane, and I. W. Hunter, "Development and performance of a controllable autoloading needle-free jet injector," *J. Med. Devices*, vol. 5, p. 015001, Mar. 2011.

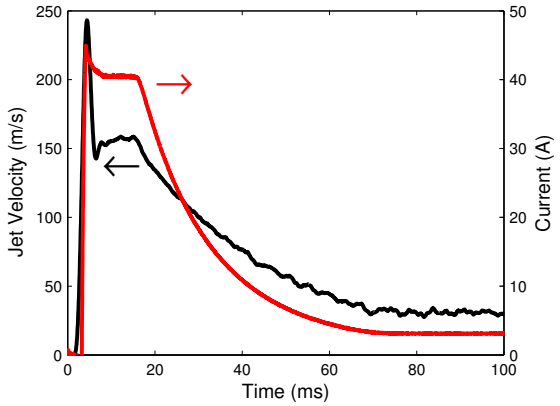

Fig. 7. The results of operating the injector from a capacitor power source controlled to 40 A maximum are shown, with the estimated jet velocity in black and the coil current in red.

[4] A. Taberner, N. C. Hogan, and I. W. Hunter, "Needle-free jet injection using real-time controlled linear Lorentz-force actuators," *Med. Eng. Phys.*, vol. 34, pp. 1228–1235, 2012.

[5] J. C. Stachowiak, T. H. Li, A. Arora, S. Mitragotri, and D. A. Fletcher, "Dynamic control of needle-free jet injection," *J. Controlled Release*, vol. 135, pp. 104–112, 2009.

[6] Y. Tagawa, N. Oudalov, A. E. Ghalbzouri, C. Sun, and D. Lohse, "Needle-free injection into skin and soft matter with highly focused microjets," *Lab Chip*, vol. 13, pp. 1357–1363, 2013.

[7] A. B. Baker and J. E. Sanders, "Fluid mechanics analysis of a spring-loaded jet injector," *IEEE Trans. Biomed. Eng.*, vol. 46, pp. 235–242, Feb. 1999.

[8] K. Chen, H. Zhou, J. Li, and G. J. Cheng, "Stagnation pressure in liquid needle-free injection: Modeling and experimental validation," *Drug Delivery Lett.*, vol. 1, pp. 97–104, 2011.

[9] R. M. J. Williams, N. C. Hogan, P. M. F. Nielsen, I. W. Hunter, and A. J. Taberner, "A computational model of a controllable needle-free jet injector," in *Proc. 34th Ann. Int. Conf. IEEE EMBS*, pp. 2052–2055, 2012.

[10] J. Schramm and S. Mitragotri, "Transdermal drug delivery by jet injectors: Energetics of jet formation and penetration," *Pharm. Res.*, vol. 19, no. 11, pp. 1673–1679, 2002.

[11] B. P. Ruddy and I. W. Hunter, "Design and optimization strategies for muscle-like direct-drive linear permanent-magnet motors.," *Int. J. Robotics Research*, vol. 30, no. 7, pp. 834–845, 2011.

[12] D. L. Trumper, W.-J. Kim, and M. E. Williams, "Design and analysis framework for linear permanent-magnet machines," *IEEE Trans. Ind. Appl.*, vol. 32, pp. 371–379, Mar. 1996.

[13] J. Wang, G. W. Jewell, and D. Howe, "A general framework for the analysis and design of tubular linear permanent magnet machines," *IEEE Trans. Magn.*, vol. 35, pp. 1986–2000, May 1999.

[14] B. P. Ruddy, *High force density linear permanent magnet motors: "electromagnetic muscle actuators"*. Ph.D. dissertation, Dept. Mech. Eng., M. I. T., Cambridge, 2012. DOI: 1721.1/78177

[15] K. Halbach, "Design of permanent multipole magnets with oriented rare earth cobalt material," *Nucl. Instrum. Methods*, vol. 169, pp. 1–10, 1980.

[16] B. P. Ruddy and I. W. Hunter, "A compact direct-drive linear synchronous motor with muscle-like performance," in *Proc. 2013 IEEE Int. Conf. Robotics and Automation (ICRA)*, pp. 1498–1503, 2013.

[17] M. Abramowitz and I. A. Stegun, Eds., *Handbook of Mathematical Functions with Formulas, Graphs, and Mathematical Tables*, 10th ed. New York: Dover, 1964.